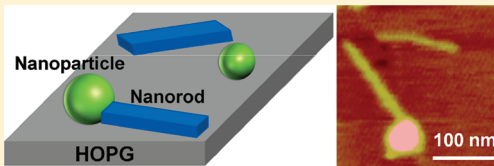


# Formation of Carboxylic Acid Nanorods on Oleylamine-Capped Au Nanoparticles

Sunxi Wang,<sup>†</sup> Li Li,<sup>†</sup> and Guangzhao Mao\*

Department of Chemical Engineering and Materials Science, Wayne State University, Detroit, Michigan 48202, United States

**ABSTRACT:** This paper describes nanorod formation induced by nanoparticle seeds. Carboxylic acids self-assemble on graphite into an epitaxial pattern. However, this persistent pattern is changed into nanorods by nanoparticles. Two control parameters have been identified, including nucleus/substrate contact angle and seed-to-critical nucleus size ratio. Effective carboxylic chain length and nanoparticle size range are identified, which can be related to the seed size effect. Some nanorods are detached when methyl-terminated nanoparticles are used, and the percentage of detached nanorods increases with increasing carbon chain length. In contrast, the nanorods do not detach from carboxyl-terminated nanoparticles. This study offers direct experimental evidence to molecular simulation prediction that nuclei display a confined morphology on a highly curved seed surface due to the difficulty of maintaining an unstrained structure and they readily detach from the surface during heterogeneous crystal nucleation. This study contributes a solution-based method for the making of nanorods.



## INTRODUCTION

Spatial control and connection of nanocomponents with distinct interfaces continue to be a major challenge in nanodevice manufacture. Template synthesis of one component in the matrix of another component is an attractive strategy for the creation of hybrid nanomaterials and nanodevices, though methods to connect individual components, such as nanoparticles and nanorods, remain few (an example being the biotinylated DNA connection to streptavidin-capped nanoparticles via molecular recognition<sup>1</sup>). Furthermore, most studies focus on inorganic materials, but self-assembly based on small organic molecules or their hybrids with inorganic nanoparticles could also yield useful properties.<sup>2</sup> Electron transfer between metal nanoparticles can be manipulated by organic interconnects in single-electron transistor (SET) devices.<sup>3</sup> Ultrasensitive electrochemical sensors based on cyclic voltammetry (CV), ion-sensitive field-effect transistors (ISFETs), or enzymatic reactions were constructed using Au nanoparticle (AuNP) superstructures with improved sensor stability, sensitivity, and selectivity.<sup>4</sup> Nanoparticle electrode materials enhanced electron transfer between redox agents and bulk electrodes and allowed fine-tuning of sensitivity via particle size, morphology, and number.<sup>5</sup> Selectivity was improved by specific interactions between the analytes and nanoparticle capping ligands.<sup>4a,6</sup> Other examples of inorganic/organic hybrid devices include AuNP-decorated  $\pi$ -conjugated nanotapes with enhanced electrical conductivity,<sup>7</sup> AuNP-decorated carbon nanotube (CNT) catalysts with higher catalytic activities toward oxygen reduction,<sup>8</sup> and enzyme-coated CNTs placed between Au electrodes showing higher enzymatic detection sensitivity.<sup>9</sup>

Our previous work showed the unique capability of certain nanoparticles to nucleate nanocrystals of extremely small cross-sectional area (nanorods) of *n*-carboxylic acids. The presence of mercaptoundecanoic acid capped cadmium selenide (MUA-

CdSe) nanoparticles was found to alter the self-assembled pattern of eicosanoic acid on highly oriented pyrolytic graphite (HOPG) from a 2-D epitaxial film to 1-D nanorods attached to the nanoparticles.<sup>10</sup> A comprehensive study of a homologous *n*-carboxylic acid series found that several of them also form nanorods readily on nanoparticles of different core materials (CdSe, CdS, and Au).<sup>11</sup> The core chemical composition is, therefore, immaterial to the nanorod formation. The chemical composition of the capping monolayer, however, plays an important role in the nanorod formation. The role of the capping layer is to provide sufficient colloidal stability for the nanoparticles to be effective nucleation seeds. It is unclear from the previous studies whether specific interactions, such as polar–polar and hydrogen-bonding interactions between the capping layer and the nucleus, are necessary for the nanorod formation. In addition, photocatalytic properties of CdSe pose a practical problem for the crystallization experiments because of the tendency of MUA-CdSe nanoparticles to aggregate over time.

To address the above issues, we employ a methyl-terminated nanoparticle whose interaction with the crystallizing unit is limited to the dispersive interaction. Oleylamine-capped AuNPs (OA-AuNPs) have been synthesized and characterized by TEM, energy dispersion spectroscopy (EDS), AFM, powder X-ray diffraction (PXRD), FTIR, and thermal gravimetric analysis (TGA). OA-AuNPs are not subjected to photoinduced aggregation, making it easier for the crystallization experiments. To compare with previous results of carboxyl-terminated nanoparticles, we use the same homologous series of *n*-carboxylic acids as crystallizing compounds and HOPG as the substrate. The results show that nanorods of carboxylic acids

Received: December 20, 2011

Revised: February 7, 2012

Published: February 10, 2012



are nucleated by OA-AuNPs with a large fraction being detached from the nanoparticles. The AFM results demonstrate that dispersive interactions alone can support the seed-mediated mechanism of nanorod formation. However, specific interactions may be necessary to maintain an intact nanoparticle/nanorod interface.

## ■ EXPERIMENTAL SECTION

**Materials.** Oleylamine (technical grade, Aldrich), hydrogen tetrachloroaurate (III) hydrate (99.9%, Strem Chemicals), and toluene (ACS grade, EMD Chemicals) were used as received. Carboxylic acids, including hexadecanoic acid ( $C_{16}A$ , Fluka,  $\geq 99.5\%$ ), eicosanoic acid ( $C_{20}A$ , Sigma,  $\geq 99\%$ ), docosanoic acid ( $C_{22}A$ , Aldrich, 99%), hexacosanoic acid ( $C_{26}A$ , Sigma,  $\geq 95\%$ ), and triacontanoic acid ( $C_{30}A$ , Sigma,  $\geq 95\%$ ), were used as received. Crystallization of the carboxylic acids was conducted in chloroform (Fisher Scientific, 100%). HOPG (Mikromasch, ZYB grade) was hand-cleaved just before use with an adhesive tape until a smooth surface was obtained.

**Nanoparticle Synthesis.** OA-AuNPs with a diameter less than 20 nm were synthesized according to the literature.<sup>12</sup> In one typical reaction, 49 mg (0.15 mmol) of HAuCl<sub>4</sub> was quickly added to a boiling solution of 10 mL (22 mmol) of oleylamine in 50 mL of toluene. After 15–30 min, the color of the solution changed gradually from bright yellow to gray yellow and finally to deep red. After 2 h heating with reflux, the reaction mixture was allowed to cool to room temperature and 100 mL of methanol was added to precipitate the product. The OA-AuNPs were isolated by centrifugation and washed three times with methanol. Vacuum drying of the precipitant yielded a black solid. The product dissolves readily in nonpolar solvents, such as chloroform.

**Film Preparation.** A 0.1 mL portion of freshly made chloroform solution of the carboxylic acid (0.1–0.4 mM) was placed on HOPG during spin-coating. In each case, the carboxylic acid concentration was adjusted depending on its solubility and solvent evaporation rate by trial and error in order to achieve near monolayer coverage. The spin rate was 3000 rpm, and the spin time was 60 s. To study the effect of the nanoparticle, 0.1 mL of freshly mixed chloroform solution containing the carboxylic acid (0.1–0.4 mM) and OA-AuNPs (0.1 mM) was used for spin-coating. The spin-coated films maintained their nanostructures for at least 1 month at room temperature.

**Characterization.** TEM (JEOL JEM-2010) and PXRD (Rigaku SmartLab) were used to determine the size distribution of the AuNP core. TEM was conducted in the bright-field mode operating at an accelerating voltage of 200 keV. The particle size was averaged over 100 individual particles measured manually by the ImageJ software. *In situ* EDS attached to the TEM was used to determine the chemical composition of the OA-AuNPs. In addition, the nanoparticles were analyzed by FTIR (PerkinElmer Spectrum 400) and TGA (Thermo Fisher Scientific).

The thin films deposited on HOPG were characterized by AFM (VEECO Dimension 3100 G scanner). Height, amplitude, and phase images were obtained in the tapping mode in ambient air. Uncoated silicon probes (TESP, VEECO) with a factory-specified spring constant of 40 N/m, length of 125  $\mu$ m, width of 40  $\mu$ m, and a nominal probe radius of curvature less than 10 nm were used. The scan rate used was in the range of 0.5–2 Hz depending on the scan size. Integral and proportional gains were approximately 0.4 and 0.8, respectively.

AFM height images are reported unless specified. Height images have been plane-fit in the fast scan direction with no additional filtering operation. Images are analyzed using the Nanoscope software from Digital Instruments (version S.12). The sectional height analysis was used to measure the vertical and lateral dimensions of the deposited nanoparticles. The lateral width was measured at the half-maximum peak height of the nanoparticle to minimize tip convolution.

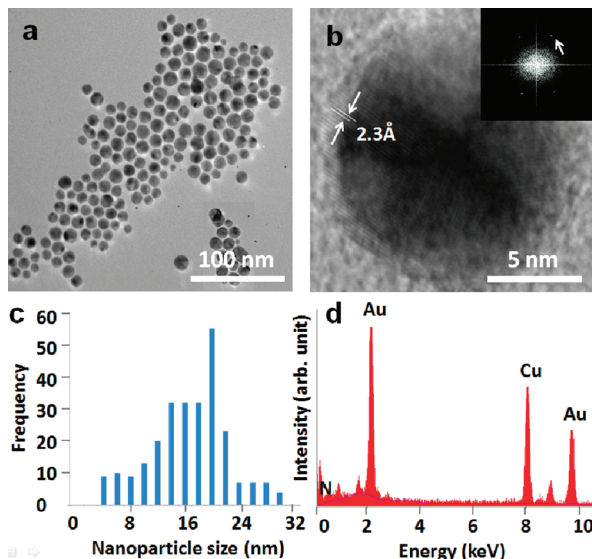
## ■ RESULTS AND DISCUSSION

**Nanoparticle Characterization.** In seed-mediated nucleation, the seed size and interfacial properties are important control parameters. The nucleation capability factor of a seed particle,  $f = (\Delta G_c^{\text{HET}})/(\Delta G_c)$ , is a function of the contact angle between the cap-shaped nucleus and the seed surface,  $\theta$ , and seed size, which can be defined as  $R' = R^S/r_c$ .<sup>13</sup>  $\Delta G_c$  and  $\Delta G_c^{\text{HET}}$  are the critical nucleation free energy for homogeneous and heterogeneous nucleation, respectively.  $R^S$  is the radius of curvature of the seed particle, and  $r_c$  is the critical nucleus radius. When the seed is large, for example,  $R' \geq 10$ , the particle surface curvature approaches that of a flat surface, and the energy barrier is dominated by  $\theta$ . When the seed is small, for example,  $R' \leq 0.1$ ,  $f$  is close to 1, and the foreign particle is ineffective in nucleation. When  $0.1 \leq R' \leq 10$ ,  $f$  decreases drastically with decreasing  $r_c$  (or increasing chemical potential difference). It suggests that small  $r_c$  or the presence of a good structural match compensating for small seed size can render nanoparticles effective nucleation seeds.

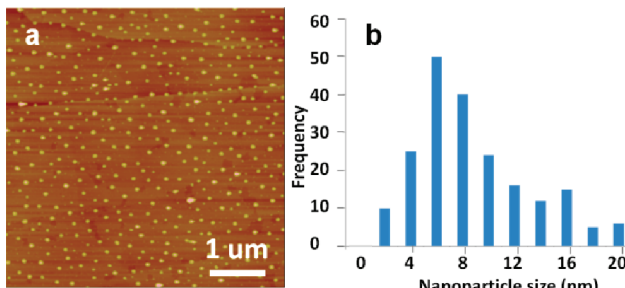
Our previous results indicate that well-dispersed nanoparticles with high colloidal stability are more likely to nucleate carboxylic acid nanorods. The data point to a seed particle size range that favors nanorod formation, and within this range, the average number of nanorods per nanoparticle is proportional to the particle surface area. Most of the previous work was conducted using nanoparticles with carboxyl termination, such as MUA-CdSe and MUA-CdS. There lacks strong evidence to show whether carboxylic acid nanorod formation requires carboxyl-terminated nanoparticle seeds, that is, specific interactions between the seed and the crystallizing agent. Here, we focus on methyl-terminated nanoparticles in the form of OA-AuNPs, and we characterize the nanoparticles by TEM, EDS, AFM, PXRD, FTIR, and TGA.

Figure 1a is a TEM image of the OA-AuNPs dispersed on the TEM copper grid. The NIH ImageJ software was used to analyze the sphericity of the particles ( $N \sim 100$ ) by measuring the area ( $A$ ) and perimeter ( $P$ ) of each particle. The average circularity of the OA-AuNPs,  $F$  ( $F = 1$  for a perfect circle), was calculated to be  $F = 4\pi A/P^2 = 0.98$ . In the following discussion, a spherical shape of the nanoparticle is assumed. Figure 1b shows a single nanoparticle with 2.3 Å fringes, consistent with the interplanar spacing of face-centered cubic (fcc) Au{111} planes. The arrow points to the reciprocal spacing in the 2D-FFT analysis (inset). Figure 1c shows the size histogram of the nanoparticles obtained from TEM images with a particle diameter range of 3–30 nm and an average diameter of  $15.7 \pm 5.6$  nm. Eighty percent of the particles are smaller than 20 nm. The atomic ratio of Au to N was determined to be  $\sim 0.25$  from the EDS spectrum (Figure 1d). The Cu signal is from the TEM sample grid.

The size distribution of OA-AuNPs was also measured using AFM. Figure 2a is a typical AFM image of OA-AuNPs on HOPG. The AFM samples were prepared by spin-coating of 0.1 mL of a 0.1 mM OA-AuNPs chloroform solution on



**Figure 1.** TEM images of OA-AuNPs at (a) low magnification ( $300 \times 300 \text{ nm}^2$ ) and (b) high magnification ( $15 \times 15 \text{ nm}^2$ ) with a 2-D FFT image as the inset. (c) Histogram of OA-AuNP diameters based on TEM. (d) EDS spectrum of OA-AuNP chemical composition.



**Figure 2.** (a) AFM image ( $z$ -range = 20 nm) of OA-AuNPs on HOPG substrate. (b) Size histogram of OA-AuNPs measured by AFM sectional height analysis.

HOPG. Chloroform quickly evaporates, leaving a uniform particle layer on HOPG. The AFM images show well-dispersed particles with no significant aggregation (a significant improvement over MUA-CdSe nanoparticles), an indication of a close-packed OA monolayer on AuNPs. Figure 2b shows the particle diameter histogram measured in the  $z$  (height) direction using AFM height images. The particle size ranges from 2 to 20 nm with an average height of  $8.2 \pm 4.1$  nm. The average OA-AuNP size by AFM is less than that measured by TEM, especially considering that AFM values include the organic capping layer. It is possible that spin-coating selectively deposits smaller particles.

OA-AuNPs were examined by PXRD, as shown in Figure 3. The X-ray peaks at  $2\theta = 38.2, 44.5, 64.6$ , and  $77.5^\circ$  correspond to  $\{111\}$ ,  $\{200\}$ ,  $\{220\}$ , and  $\{311\}$  crystalline planes with the interplanar  $d$ -spacing of  $2.35, 2.03, 1.44$ , and  $1.23 \text{ \AA}$ , respectively. The intrinsic crystalline domain size,  $\tau$ , was estimated using the Scherrer equation,  $\tau = (K\lambda)/(\beta \cos \theta)$ , where  $K$  is the shape factor equaling 0.9 for a single crystal with a spherical shape,  $\lambda$  is the Cu  $K\alpha$  wavelength, and  $\beta$  is the full width at half-maximum peak height. The estimated diameters of OA-AuNPs using four individual peaks are 18.7, 12.5, 14.1, and 13.0 nm, respectively, and the average is 14.6 nm.

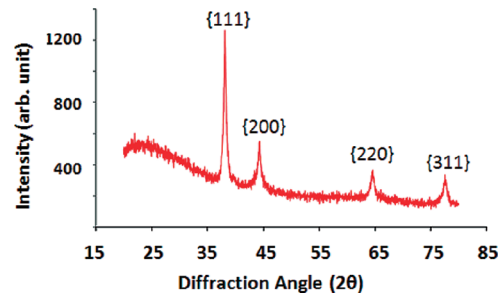


**Figure 3.** PXRD pattern of OA-AuNPs.

Figure 4 shows the FTIR spectra of oleylamine (blue) and OA-AuNPs (red). Both spectra display the characteristic C–H

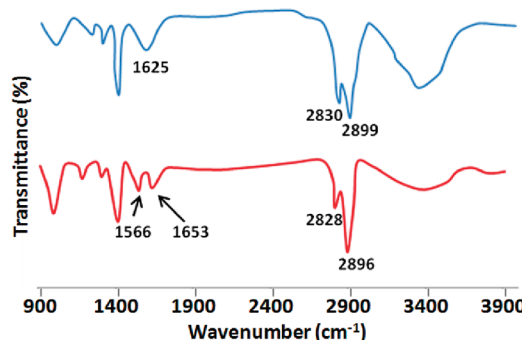


**Figure 4.** FTIR spectra of OA (blue) and OA-AuNPs (red) powders.

stretching vibration frequencies,  $\sim 2830$  and  $2900 \text{ cm}^{-1}$ . After the reaction, the N–H bending peak at  $1625 \text{ cm}^{-1}$  disappears and new peaks associated with the amide bond,  $1566$  and  $1653 \text{ cm}^{-1}$ , appear. Our results, consistent with those of others,<sup>14</sup> indicate that oxidation of oleylamine to oleylamine (Figure 5) accompanies the reduction of Au(III) to Au(0). The hydrogen bond formation among the amide groups improves the monolayer chemical stability. The OA-AuNPs dissolve readily in chloroform. We conclude that the OA-AuNPs are terminated by the methyl group, rendering them hydrophobic.

To determine the surface coverage of the OA monolayer on AuNPs, TGA measurements were conducted, as shown by Figure 6. The weight loss from 100 to  $375^\circ\text{C}$  is attributed to the burnoff of the organic OA layer. The measured weight loss, 3.5% of the initial sample weight, corresponds to a molar ratio of Au to oleylamine of 39.5. In contrast, Au/N is 0.25 according to the EDS analysis. EDS overestimates the percentage of elemental N due to environmental impurities. The OA monolayer coverage on the AuNP surface in area per OA molecule is calculated to be  $27.6 \text{ \AA}^2$  using the average diameter of a AuNP ( $=14.6 \text{ nm}$  from PXRD), Au/OA molar ratio ( $=39.5$  from TGA), and density of Au ( $=19.3 \text{ g/cm}^3$ ). For comparison, the limiting area per molecule for *n*-alkyl derivatives, including carboxylic acids, amines, amides, and alcohols, is  $20\text{--}22 \text{ \AA}^2$ . The highest coverage of MUA on CdSe nanoparticles in our previous work yields an area per thiolate of  $29.8 \text{ \AA}^2$ .<sup>11</sup>

**Film Structure of *n*-Carboxylic Acids on HOPG.** Alkanes and alkane derivatives, such as *n*-carboxylic acids, physisorb on HOPG with their carbon chain skeletal plane parallel to the HOPG basal plane.<sup>16</sup> AFM studies of  $C_{14\text{--}26}A$ 's spin-coated from alcoholic solvents showed a double-chain structure with a periodicity twice the molecular chain length on HOPG.<sup>10,11</sup>  $C_{30}A$ , on the other hand, displayed an additional single-chain

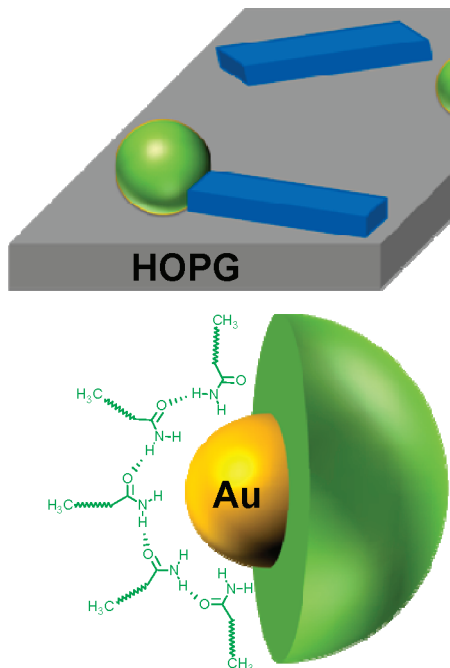


**Figure 5.** Nanoparticle/nanorod hybrid system generated by seed-mediated nucleation. The nanoparticle consists of a core–shell structure with a Au core and a H-bonded oleylamide monolayer shell. *n*-Carboxylic acid nanorods nucleated by the OA-AuNP have a tendency to detach from the nanoparticle.

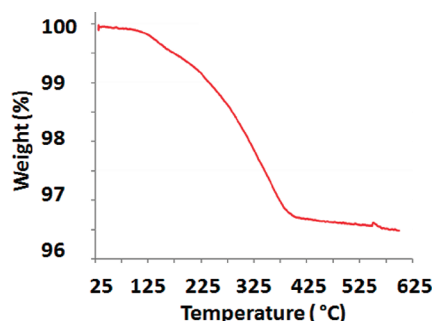


**Figure 6.** TGA graph of OA-AuNPs.

domain with one-half of the double-chain periodicity. When switching the solvent from the ethanolic type to chloroform, the film nanostructures of  $C_{16-30}A$ 's on HOPG were found to be largely unchanged. Figure 7 shows typical AFM images of the carboxylic acids' films. The periodicity values of the double-chain domain pattern for  $C_{16}A$ ,  $C_{20}A$ ,  $C_{22}A$ ,  $C_{26}A$ , and  $C_{30}A$  are reported in Table 1.  $C_{30}A$  forms an additional single-chain domain with a periodicity of 3.9 nm. The film thickness is  $0.3 \pm 0.1$  nm, indicating a monolayer structure in which the carbon skeleton plane of the carboxylic acid lies parallel to the HOPG basal plane.

**Film Structure of *n*-Carboxylic Acids on HOPG in the Presence of OA-AuNPs.** To address the question of whether the carboxylic nanorod formation requires a seed surface with the carboxyl group, a series of experiments were carried out using methyl-terminated OA-AuNPs in chloroform. Figure 8 summarizes the results of  $C_{16-30}A$ 's film structure in the presence of OA-AuNPs on HOPG. The dimensions of the nanorods by AFM height sectional analysis are reported in Table 1. The nanorod structure is identical to the one induced

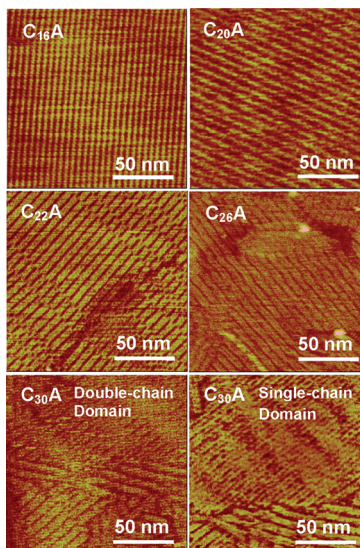


**Figure 7.** AFM height images of  $C_{16-26}A$  and  $C_{30}A$  monolayers with a double-chain domain and phase image for  $C_{30}A$  monolayers with a single-chain domain on HOPG. The  $z$ -range is 1 nm for  $C_{16-26}A$  and  $C_{30}A$  with a double-chain domain and 5° for  $C_{30}A$  with a single-chain domain.

**Table 1. AFM Results of the Periodicity of Carboxylic Acid Stripe Patterns and the Height and Width of Carboxylic Acid Nanorods**

carboxylic acid	periodicity by AFM (nm)	height of nanorods (nm)	width of nanorods (nm)
$C_{16}A$	4.7	$0.8 \pm 0.2$	$10.9 \pm 2.4$
$C_{20}A$	5.6	$0.8 \pm 0.3$	$7.0 \pm 1.7$
$C_{22}A$	6.1	$1.1 \pm 0.4$	$7.8 \pm 2.3$
$C_{26}A$	7.0	$1.0 \pm 0.3$	$10.0 \pm 2.1$
$C_{30}A$	8.0	$0.8 \pm 0.2$	$11.4 \pm 2.6$

by MUA-CdSe nanoparticles, which displays the characteristic dimensions of the C-form carboxylic acid crystal structure that exists in all these systems. No nanorods were obtained with carboxylic acids with fewer than 16 carbons. These shorter molecules formed a 2-D layer around the nanoparticles. Carboxylic acids with more than 30 carbons were not studied. The C-form crystal structure of  $C_{18}A$  ( $P2_1/a$ ,  $Z = 4$ ) has the following lattice parameters:  $a = 0.9360$  nm,  $b = 0.4950$  nm,  $c = 5.0700$  nm, and  $\beta = 128.250^\circ$ .<sup>17</sup> The individual nanorods display a fixed height,  $\sim 1$  nm, a width close to twice the chain length, and a stochastic length distribution in the range of 50–250 nm. The width of  $C_{20-30}A$ 's nanorods is  $\sim 2.6$  times the respective chain length, an apparent value due to tip convolution. The width of  $C_{16}A$  nanorods is  $\sim 5$  times its chain length, suggesting the formation of nanorod doublets.<sup>11</sup> By comparing the nanorod dimensions and its expected crystal structure, we conclude that the nanorods are formed by carboxylic acid unit cells attaching to each other along the  $b$  direction in the C-form crystal structure during crystallization. The carboxylic acid nanorod possesses the unit cell dimensions (the smallest crystalline unit) in both width and height directions, and it consists of a single bilayer row in the width direction with a H-bonded carboxyl group in the center and terminal methyl groups at the sides. Our data also show a roughly 1:1 ratio between the nanoparticle and the nanorod,

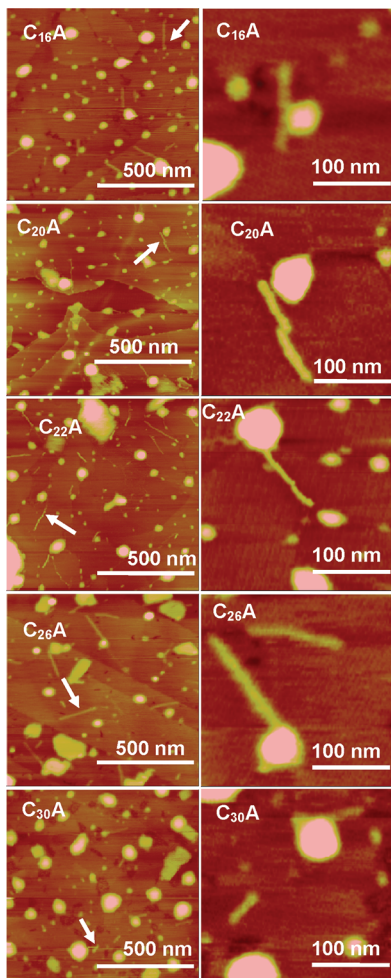


**Figure 8.** Low-magnification (left column,  $z$ -range = 10 nm) and high-magnification (right column,  $z$ -range = 5 nm) AFM height images of *n*-carboxylic acids on HOPG in the presence of OA-AuNPs.

which is consistent with the nanoparticle-mediated nanorod formation mechanism.

Other observations consistent with the MUA-CdSe case are summarized here. (1) There is a seed size range that favors nanorod formation, in this case, seeds with a height of 4–10 nm (Figure 9). 2-D stripe layer domains form around nanoparticles larger than 10 nm in height. This is understood partially by the classical nucleation treatment of the nucleation energy barrier as a function of seed size and interfacial energies (or contact angle).<sup>13</sup> Small seeds are ineffective nucleation

agents because they do not lower the nucleation energy. The effect of large seeds is dominated by the contact angle with diminishing curvature effect. In addition, interfacial strain arising from a highly curved interface, that is, the surface of a small nanoparticle, may promote 1-D nanorod growth and suppress 2-D layer growth. (2) For the longest chain,  $C_{30}A$ , the fewest nanorods are observed (Figure 7). In the competition between HOPG- and nanoparticle-mediated molecular ordering, longer carbon chain length favors the epitaxial interaction with HOPG because the epitaxial interaction with HOPG increases with increasing chain length. Thus, the epitaxial mismatch between the HOPG lattice and carboxylic acid molecules in the randomly oriented nanorods nucleated from the nanoparticle becomes increasingly prohibitive for nanorods composed of longer chains. Instead, they self-assemble into the nanostripe pattern on HOPG.

Major differences between the nanorods induced by OA-AuNPs and those produced by MUA-CdSe<sup>10,11</sup> are that (1) fewer nanorods are produced by OA-AuNPs, (2) OA-AuNPs do not support multiple rods per particle (the percentage of multiple rods per MUA-CdSe increases with increasing particle size), and (3) a large percentage of the nanorods produced by OA-AuNPs are detached from the seed (arrows pointing to this feature in Figure 8). The results show that the OA-AuNP has a lower nucleation capability of nanorods than the MUA-CdSe. The percentage of detached nanorods of all nanorods formed was found to increase with increasing chain length. The percentage of detached nanorods is 22% for  $C_{16}A$ , 26% for  $C_{20}A$ , 55% for  $C_{22}A$ , and 74% for  $C_{26}A$ . There are not enough nanorods for meaningful statistical evaluation in the case of  $C_{30}A$ . The percentage of detached nanorods is not affected by the spin speed. Among the attached nanorods, there is roughly an equal number of nanorods oriented along the radial direction and tangential direction to the nanoparticle surface. The similar distribution of the two orientations is consistent with an equal attachment probability of carboxyl dimers in the tangential and radial orientations to the particle seed surface. The similar size of the tangentially oriented nanorods and the radially oriented nanorods suggests that, at least in this case, the strain energy caused by misalignment of carboxylic acid nanorods on carboxylic acid monolayer-covered HOPG plays the more dominant role in limiting the crystal growth width direction than the curvature constraint placed by the nanoparticle. In contrast, carboxylic acid nanorods are almost always found to be attached to MUA-CdSe nanoparticles. In a molecular dynamics simulation study of seed-mediated colloidal crystallization,<sup>15</sup> elongated colloidal clusters form on the seed particle surface when the seed particle radius is at 5 times the size of the colloidal particles. Molecular simulations predict a transition of nucleating clusters from an elongated “1-D” shape to 2-D shell wrapping around the seed when the seed-to-nucleating compound size ratio changes from 5 to 7. The authors hypothesize that the radially elongated cluster is induced by the high curvature of the small seed, which imposes an unsustainable strain for tangential growth. Although the length scale of our system may not be pertinent to the colloidal crystallization simulated, our observations of the 1-D rods and 1-D to 2-D transition as a function of seed particle size are consistent with the 1-D clusters in the simulations. Snapshots show a transition from attached clusters to detached clusters during the nucleation process. An implication of this cluster detachment from the seed particle is that heterogeneous nucleation could still be the primary nucleation mechanism

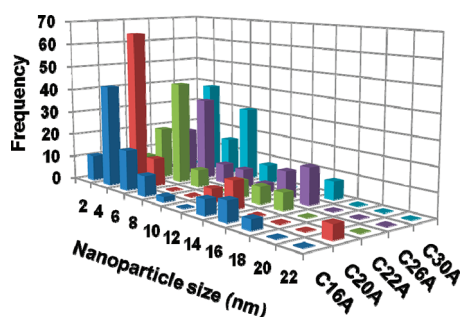


**Figure 9.** Histogram of the percentage (%) of nanorods induced by nanoparticles as a function of the height of the nanoparticles.

even in cases when nuclei are only observed in bulk. Our observation of detached carboxylic acid nanorods provides experimental evidence of nuclei detaching from the seed surface predicted by the molecular simulation. One possible reason for the detached nanorods in the OA-AuNP case may be the lower interfacial bonding energy between the nanorod and the alkyl group at the surface of the OA-AuNP as compared with that between the same nanorod and carboxyl-terminated MUA-CdSe nanoparticles. In the latter case, polar–polar and hydrogen-bonding interactions are likely present to prevent nanorod detachment from the seed surface.

## CONCLUSIONS

The work demonstrates a methodology of using monolayer-protected inorganic nanoparticles as nucleation seeds for the creation of extremely narrow organic nanorods. OA-AuNPs of high colloidal stability are synthesized and characterized by AFM, TEM, XRD, EDS, FTIR, and TGA. Homologous carboxylic acid films deposited on HOPG in the absence and presence of OA-AuNPs are studied by AFM. Carboxylic acids with different chain lengths self-assemble into a stripe nanopattern on HOPG due to favorable epitaxial interactions between the carbon chains and the HOPG crystalline lattice. This persistent nanopattern is perturbed by the presence of OA-AuNPs, and nanorods with random orientations are produced. The narrow width of the nanorod is attributed to two energetic factors. There is a significant mismatch between the carbon chain plane and HOPG for randomly oriented nuclei, which prevents the attachment of carboxyl dimers along the carbon chain direction (the *c* axis). The second factor is the high strain energy as a result of the highly curved surface of the nanoparticle in the tangential direction of the seed surface. This work shows that specific interactions between the seed surface and the crystalline compound are unnecessary for the nanorod formation since nanorods of identical structures are produced by methyl-terminated nanoparticles. However, the tendency of nanorods to detach from the methyl-terminated nanoparticle surface points to the role of specific (polar/polar or hydrogen-bonding) interactions in maintaining an intact nanoparticle and nanorod interface in seed-mediated nucleation.

## AUTHOR INFORMATION

### Corresponding Author

\*E-mail: gzmao@eng.wayne.edu.

### Author Contributions

<sup>†</sup>These authors contributed equally to this work.

### Notes

The authors declare no competing financial interest.

## ACKNOWLEDGMENTS

We acknowledge the financial support from the National Science Foundation (CBET-0553533, CBET-0619528, and CBET-0755654). We thank Rita Andrews from BASF Corporation, Wyandotte, Michigan, for conducting the TGA measurements.

## REFERENCES

- (1) Niemeyer, C. M. Nanoparticles, proteins, and nucleic acids: Biotechnology meets materials science. *Angew. Chem., Int. Ed.* **2001**, *40* (22), 4128–4158.
- (2) (a) Leclerc, P.; Surin, M.; Jonkheijm, P.; Henze, O.; Schenning, A. P. H. J.; Biscarini, F.; Grimsdale, A. C.; Feast, W. J.; Meijer, E. W.;

Mullen, K.; Bredas, J. L.; Lazzaroni, R. Organic semi-conducting architectures for supramolecular electronics. *Eur. Polym. J.* **2004**, *40* (5), 885–892. (b) Mullen, K.; Rabe, J. P. Macromolecular and supramolecular architectures for molecular electronics. *Molecular Electronics: Science and Technology*; The New York Academy of Sciences: New York, 1998; Vol. 852, 205–218. (c) Ruaudelteixier, A. Supramolecular Assemblies for Molecular Electronics. *Mol. Cryst. Liq. Cryst. Sci. Technol., Sect. A* **1994**, *255*, 27–33. (d) Schenning, A. P. H. J.; Jonkheijm, P.; Hoeben, F. J. M.; van Herrikhuyzen, J.; Meskers, S. C. J.; Meijer, E. W.; Herz, L. M.; Daniel, C.; Silva, C.; Phillips, R. T.; Friend, R. H.; Beljonne, D.; Miura, A.; De Feyter, S.; Zdanowska, M.; Uji-i, H.; De Schryver, F. C.; Chen, Z.; Wurthner, F.; Mas-Torrent, M.; den Boer, D.; Durkut, M.; Hadley, P. Towards supramolecular electronics. *Synth. Met.* **2004**, *147* (1–3), 43–48. (e) Schenning, A. P. H. J.; Meijer, E. W. Supramolecular electronics; nanowires from self-assembled  $\pi$ -conjugated systems. *Chem. Commun.* **2005**, No. 26, 3245–3258.

(3) Feldheim, D. L.; Keating, C. D. Self-assembly of single electron transistors and related devices. *Chem. Soc. Rev.* **1998**, *27* (1), 1–12.

(4) (a) Shipway, A. N.; Katz, E.; Willner, I. Nanoparticle arrays on surfaces for electronic, optical, and sensor applications. *ChemPhysChem* **2000**, *1* (1), 18–52. (b) Zabet-Khosousi, A.; Dhirani, A. A. Charge transport in nanoparticle assemblies. *Chem. Rev.* **2008**, *108* (10), 4072–4124.

(5) Wu, Y.; Cheng, G.; Katsov, K.; Sides, S. W.; Wang, J.; Tang, J.; Fredrickson, G. H.; Moskovits, M.; Stucky, G. D. Composite mesostructures by nano-confinement. *Nat. Mater.* **2004**, *3* (11), 816–822.

(6) (a) Israel, L. B.; Kariuki, N. N.; Han, L.; Maye, M. M.; Luo, J.; Zhong, C. J. Electroactivity of  $Cu^{2+}$  at a thin film assembly of gold nanoparticles linked by 11-mercaptopoundecanoic acid. *J. Electroanal. Chem.* **2001**, *517* (1–2), 69–76. (b) Riskin, M.; Tel-Vered, R.; Bourenko, T.; Granot, E.; Willner, I. Imprinting of molecular recognition sites through electropolymerization of functionalized Au nanoparticles: Development of an electrochemical TNT sensor based on  $\pi$ -donor-acceptor interactions. *J. Am. Chem. Soc.* **2008**, *130* (30), 9726–9733. (c) Krasteva, N.; Besnard, I.; Guse, B.; Bauer, R. E.; Mullen, K.; Yasuda, A.; Vossmeyer, T. Self-assembled gold nanoparticle/dendrimer composite films for vapor sensing applications. *Nano Lett.* **2002**, *2* (5), 551–555.

(7) van Herrikhuyzen, J.; George, S. J.; Vos, M. R. J.; Sommerdijk, N. A. J. M.; Ajayaghosh, A.; Meskers, S. C. J.; Schenning, A. P. H. J. Self-assembled hybrid oligo(*p*-phenylenevinylene)–Gold nanoparticle tapes. *Angew. Chem., Int. Ed.* **2007**, *46* (11), 1825–1828.

(8) Shi, Y.; Yang, R. Z.; Yuet, P. K. Easy decoration of carbon nanotubes with well dispersed gold nanoparticles and the use of the material as an electrocatalyst. *Carbon* **2009**, *47* (4), 1146–1151.

(9) Besteman, K.; Lee, J. O.; Wiertz, F. G. M.; Heering, H. A.; Dekker, C. Enzyme-coated carbon nanotubes as single-molecule biosensors. *Nano Lett.* **2003**, *3* (6), 727–730.

(10) Chen, D.; Wang, R.; Arachchige, I.; Mao, G.; Brock, S. L. Particle-rod hybrids: Growth of arachidic acid molecular rods from capped cadmium selenide nanoparticles. *J. Am. Chem. Soc.* **2004**, *126* (50), 16290–16291.

(11) Wang, R.; Li, L.; Arachchige, I.; Ganguly, S.; Brock, S. L.; Mao, G. Nanoparticles change the ordering pattern of *n*-carboxylic acids into nanorods on HOPG. *ACS Nano* **2010**, *4* (11), 6687–6696.

(12) Hiramatsu, H.; Osterloh, F. E. A simple large-scale synthesis of nearly monodisperse gold and silver nanoparticles with adjustable sizes and with exchangeable surfactants. *Chem. Mater.* **2004**, *16* (13), 2509–2511.

(13) (a) Fletcher, N. H. Size effect in heterogeneous nucleation. *J. Chem. Phys.* **1958**, *29* (3), 572–576. (b) Liu, X. Y. *Generic Mechanism of Heterogeneous Nucleation and Molecular Interfacial Effects*. Elsevier Sci. B. V.: Amsterdam, 2001. (c) Liu, X. Y. Generic Progressive Heterogeneous Processes in Nucleation. *Langmuir* **2000**, *16* (18), 7337–7345.

(14) Huo, Q.; Liu, X.; Atwater, M.; Wang, J. H.; Dai, Q.; Zou, J. H.; Brennan, J. P. A study on gold nanoparticle synthesis using oleylamine

as both reducing agent and protecting ligand. *J. Nanosci. Nanotechnol.* **2007**, *7* (9), 3126–3133.

(15) Cacciuto, A.; Auer, S.; Frenkel, D. Onset of heterogeneous crystal nucleation in colloidal suspensions. *Nature* **2004**, *428* (6981), 404–406.

(16) (a) Rabe, J. P.; Buchholz, S. Commensurability and Mobility in 2-Dimensional Molecular-Patterns on Graphite. *Science* **1991**, *253* (5018), 424–427. (b) Kuroda, R.; Kishi, E.; Yamano, A.; Hatanaka, K.; Matsuda, H.; Eguchi, K.; Nagagiri, T. Scanning tunneling microscope images of fatty acid Langmuir-Blodgett bilayers. *J. Vac. Sci. Technol. B* **1991**, *9* (2), 1180–1183. (c) Kishi, E.; Matsuda, H.; Kuroda, R.; Takimoto, K.; Yamamo, A.; Eguchi, K.; Hatanaka, K.; Nakagiri, T. Barrier-Height Imaging of Fatty-Acid Langmuir-Blodgett-Films. *Ultramicroscopy* **1992**, *42*, 1067–1072. (d) Hibino, M.; Sumi, A.; Tsuchiya, H.; Hatta, I. Microscopic Origin of the Odd-Even Effect in Monolayer of Fatty Acids Formed on a Graphite Surface by Scanning Tunneling Microscopy. *J. Phys. Chem. B* **1998**, *102* (23), 4544–4547. (e) Mao, G.; Dong, W.; Kurth, D. G.; Mohwald, H. Synthesis of Copper Sulfide Nanorod Arrays on Molecular Templates. *Nano Lett.* **2004**, *4* (2), 249–252.

(17) (a) Kaneko, F. *Crystallization Processes in Fats and Lipid Systems*; Garti, N., Sato, K., Eds.; Marcel Dekker: New York, 2001; 53–97. (b) Malta, V.; Celotti, G.; Zannetti, R.; Martelli, A. F. Crystal structure of the C form of stearic acid. *J. Chem. Soc. B* **1971**, 548–553. (c) CCDC STARAC01 contains the supplementary crystallographic data of stearic acid C-form. It can be obtained free of charge via [www.ccdc.cam.ac.uk](http://www.ccdc.cam.ac.uk/data_request/cif).